Molecular Engineering of Emissive Molecular Qubits Based on Spin-Correlated Radical Pairs

Neo Lin[1,5], Miu Tsuji[1,5], Isabella Bruzzese[1], Angela Chen[1], Michael Vrionides[1], Noen Jian,[1] Farhan Kittur[1,2], Thomas P. Fay[3], and Tomoyasu Mani[1,4]*

[1]Department of Chemistry, University of Connecticut, Storrs, CT

[2]Glastonbury High School, Glastonbury, CT

[3]Aix Marseille Univ, CNRS, ICR, 13397 Marseille, France

[4]Chemistry Division, Brookhaven National Laboratory, Upton, NY

[5]These authors contributed equally: Neo Lin, Miu Tsuji.

*tomoyasu.mani@uconn.edu, tmani@bnl.gov

Abstract

Spin chemistry of photogenerated spin-correlated radical pairs (SCRPs) offers a practical approach to control chemical reactions and molecular emissions using weak magnetic fields. This capability to harness magnetic field effects (MFEs) paves the way for developing SCRPs-based molecular qubits. Here, we introduce a new series of donor-chiral bridge-acceptor (D-χ-A) molecules that demonstrate significant MFEs on fluorescence intensity and lifetime in solution at room temperature – critical for quantum sensing. By precisely tuning the donor site through torsional locking, distance extension, and planarization, we achieved remarkable control over key quantum properties, including field-response range and linewidth. In the most responsive systems, emission lifetimes increased by over 200%, and total emission intensity was modulated by up to 30%. This level of tunability, and rational design principle of optically addressable molecular qubits, represents a major leap toward functional synthetic molecular qubits, advancing the field of molecular quantum technologies.

Main

Molecular qubits are crucial in advancing quantum information science and technology (QIST). Among the various molecular qubits, spin-correlated radical pairs (SCRPs), based on organic molecules, provide a unique platform with long coherence time (100s of nanoseconds at room temperature), chemical tunability, and operation at room and higher temperatures.[1, 2, 3] These SCRPs form through photoinduced charge separation (CS), with entangled electronic spins sensitive to external magnetic fields, functioning as spin qubit pairs.[4] Optical addressability is crucial for applications in quantum sensing. NV (nitrogen-vacancy) centers are color centers that can report a spin state of qubits by emission.[5] Mimicking the function of NV centers, metal-based molecular qubits such as chromium (Cr^{4+})[6] and vanadium (V^{3+})[7] can work as molecular color centers.[8, 9]

We previously showed that we can also design donor-bridge-acceptor (D-B-A) molecules whose emission can be controlled by magnetic fields through SCRPs in solutions at room temperature, albeit the changes were small.[10] The basic photophysical scheme of such systems is shown in **Fig. 1a**, where an emissive acceptor molecule is photoexcited (^{S}A*). In this scheme, SCRPs are produced as a singlet from ^{S}A*. Without a strong perturbation (i.e., spin-orbit couplings), singlet RPs recombine to form local singlet states, while local triplet excited states (triplets) cannot form. Singlet or triplet RPs can evolve coherently and interconvert through a process called radical pair intersystem crossing (RP-ISC) that is driven by hyperfine coupling.[11] As the spin-selective recombination rates are usually different for singlet and triplet RPs, applied magnetic fields can alter the lifetime of RPs by modifying their singlet-triplet character, therefore changing the relative contributions of the respective recombinations to the overall kinetics. Such modulation is possible by weak magnetic fields (<1 Tesla),[11] 3-4 orders of magnitude smaller than the thermal energy k_BT at room temperature (≈25 meV) and 5-6 orders of magnitude smaller than the molecular emission. As the emissive state (^{S}A*) is regenerated by spin-selective recombination (bCR), this emission reports spin changes in the SCRPs, specifically addressing the singlet RP (**Fig. 2a**). High magnetic sensitivity in emission intensity based on SCRPs-associated emission was previously achieved by exciplex emission from donor/acceptor molecules connected with flexible linkers using UV-excitable molecules.[12, 13] Cohen and co-workers applied these types of molecules in the microscopic imaging of magnetic inhomogeneities.[14, 15] In principle, one could develop molecular quantum technologies like super-resolution tomography, microscopy, and quantum control of chemical reactions. Yet, there is a significant gap between the theory and experiments.[3]
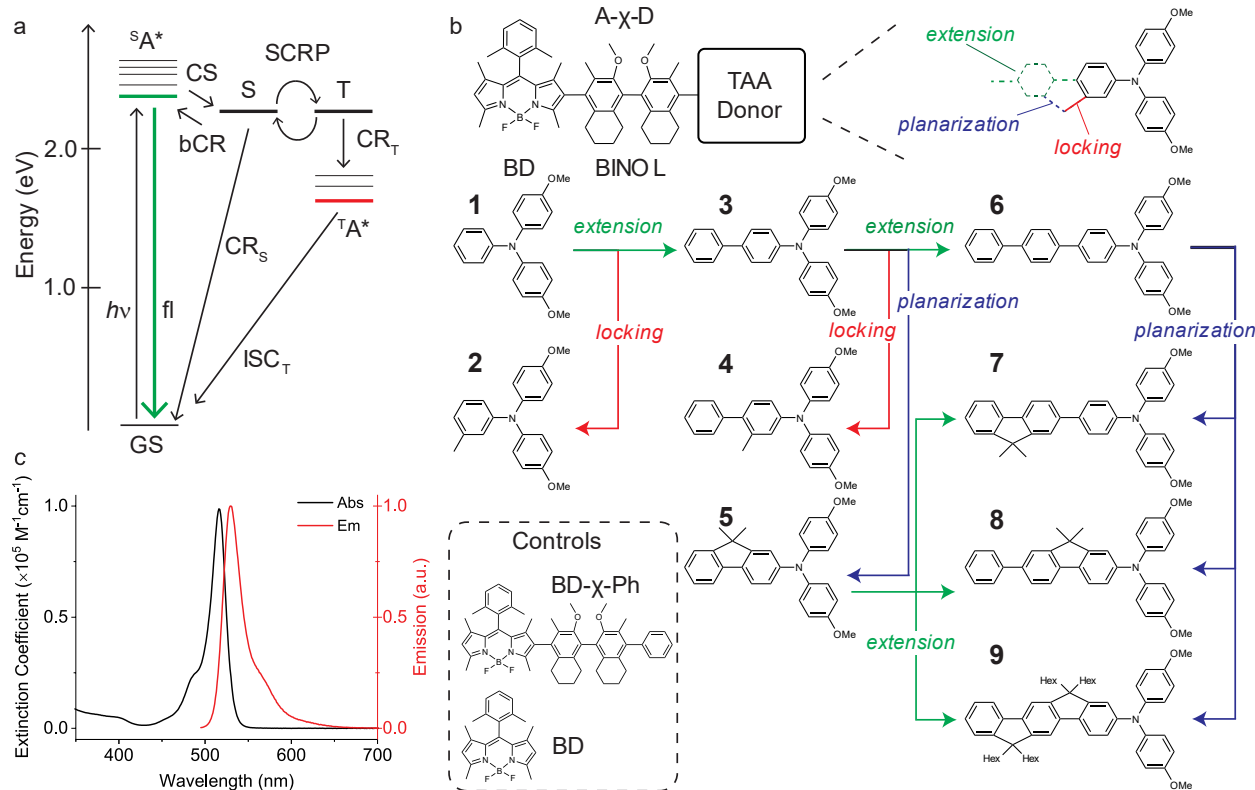
Fig. 1: Molecular engineering of emissive SCRPs-based molecular qubits. **a**, Photophysical pathways of emissive molecular qubits based on SCRPs. **b**, Molecular structures of new D-χ-A molecules where A is BODIPY, χ is a BINOL derivative, and D is triarylamines (TAA). Note that the chirality of BINOL is *R* except for **7** and **8**, which are *S*. Inset shows the two control molecules. **c**, Representative absorption and emission (λ$_{ex}$ = 480 nm) spectra of a D-χ-A molecule (**1**) in anisole.

Here, we present a new series of D-χ-A molecules that exhibit unprecedented magnitude of MFEs on recombination fluorescence where χ is a chiral bridge molecule (**Fig. 1b**). We identified that a 1,1'-Bi-2-naphthol (BINOL) derivative serves as a bridge, providing sufficient electronic couplings for long-lived SCRPs necessary for efficient spin mixing and magnetic modulations. A similar chiral bridge was recently used[16, 17] to study chirality induced spin selectivity (CISS) effect.[18] We tested the synthetic tunability, considered as a hallmark of molecular qubits.[1] We systematically modified the donor site through torsional locking, distance extension, and planarization while keeping the χ-A motif intact. This molecular engineering enables us to adjust the spin and magnetic properties such as the field-response range and linewidth in a systematic manner. The observed magnetic sensitivity showcases a remarkable increase of >200% in emission lifetimes,

reaching up to 30% modulation of total emission intensity. This work lays the concrete foundations to synthetically tune the emissive molecular qubits, contributing to the developments of molecular quantum technologies.

Results and discussion

Molecular design and synthesis

We hypothesized that structurally hindered biphenyls like BINOL provides adequate coupling to promote charge separation while preventing rapid recombination. The synthetic scheme is shown in Supplementary Information. Nuclear magnetic resonance (NMR) spectroscopy and mass spectroscopy established the identity and purity of these molecules. Though two stereoisomers are possible (*syn* vs *anti*, Supplementary Fig. 1), we did not isolate them, and NMR showed no distinct signatures of each isomer. Synthesis procedures and characterizations are in Supplementary Information. Molecule **1** is a basis among the D-χ-A series, while **BD-χ-Ph** and **BD** are the control molecules (**Fig. 1b** inset).

All the molecules show characteristic BODIPY absorption and emission bands at λ_{max} = 516 nm and 530 nm, respectively (**Fig. 1c**, Supplementary Fig. 2). Circular dichroism (CD) confirms the presence of chiral BINOLs, with some CD signals indicating electronic couplings between BODIPY and BINOL, though weaker than previously reported BODIPY-BINOL complexes.[19] This is due to the nearly orthogonal π-planes (Supplementary Figs. 3-4). The BODIPY's initial excited state of D-χ-A is E_{S1} = 2.37 eV, slightly lower than **BD** (2.43 eV), with a red-shifted absorption band typical for β-coupled BODIPYs.[20] The extinction coefficient is $\varepsilon \approx 10^5$ $M^{-1}cm^{-1}$ (Supplementary Table 1).

Time-resolved emission measurements reveal long-lived recombination fluorescence (τ ~50 – 100 ns) in addition to the prompt fluorescence (Supplementary Fig. 5). Femtosecond transient absorption (fsTA) measurements confirmed the production of RPs (BD$^{\bullet-}$-BINOL-TAA$^{\bullet+}$, Supplementary Figs. 6-16, Supplementary Note 1). The equilibrium between S1 and singlet RP was confirmed by temperature-dependent emission measurements (Supplementary Fig. 17). The lifetime of recombination fluorescence reflects the total lifetime of RPs, which is confirmed by nanosecond transient absorption (nsTA) spectroscopy. Some RPs recombine to form the triplet excited state of BODIPY (T1), whose lifetime is ~ 300 μs in deoxygenated anisole (Supplementary Fig. 18). TA and emission lifetime measurements provide the rates of electron transfer processes (Supplementary Table 2). Basic photophysical characterizations are reported in **Table 1**. We used the three-state model (Supplementary Note 2)[21] to fit the double exponential fluorescence decay

to experimentally determine the Gibbs energy changes associated with the charge separation and recombination (**Table 1**, Supplementary Table 4). We also characterized the molecules electrochemically. The cyclic voltammetry (CV) data are reported in Supplementary Table 3, Supplementary Fig. 19-20. The spectroelectrochemical data of the radical cations (Supplementary Fig. 21, Supplementary Table 5) support the assignments of the TA data.

Table 1 Emissive parameters of the new D-χ-A molecules and two control molecules in anisole in the absence of magnetic fields.[a]

	Donor	r_{DA} (Å)[b]	ΔG_{CS} (eV)[c]	Φ_{em}[c]			τ_{em}[c] (ns)		Φ_T
				Total	Prompt	RF	Prompt	RF[d]	
1	TPA	17.8	-0.15	0.57	0.23	0.34	1.34	105 (27)	0.15
2	MeTPA	17.8	-0.14	0.39	0.28	0.11	1.65	103 (26)	0.24
3	PhTPA	21.7	-0.11	0.78	0.72	0.06	3.40	52 (23)	0.09
4	PhMeTPA	21.9	-0.10	0.85	0.84	0.01	3.84	62 (34)	0.07
5	FDPA	21.0	-0.14	0.37	0.29	0.08	1.80	96 (26)	0.27
6	Ph₂TPA	25.8	-0.11	1.0	0.99	0.01	4.27	97 (75)	0.02
7	FPhDPA	25.0	-0.11	0.82	0.80	0.02	4.08	50 (43)	0.09
8	PhFDPA	25.1	-0.15	0.94	0.92	0.02	4.00	53 (48)	0.05
9	iFDPA	24.6	-0.14	0.47	0.35	0.12	3.79	64 (23)	0.22
BD-χ-Ph[e]	NA	NA	NA	1.0	1.0	NA	4.42	NA	0
BD[e]	NA	NA	NA	1.0	1.0	NA	4.92	NA	0

[a] The values are reported for deoxygenated solutions unless otherwise noted. [b] Based on the DFT-optimized structures at B3LYP/6-31g+(d)/CPCM (anisole). [c] Three-state fit of the emission lifetime (Supplementary Information). [d] The values in the parenthesis are the lifetimes in non-deoxygenated solutions. [e] No charge transfer processes occur, and Φ_T is negligible.

Magnetic modulation of emissivity and dark states

We observed a change in emission intensity upon switching on the magnetic field (e.g., **2** in **Fig. 2b**). The changes are reversible.
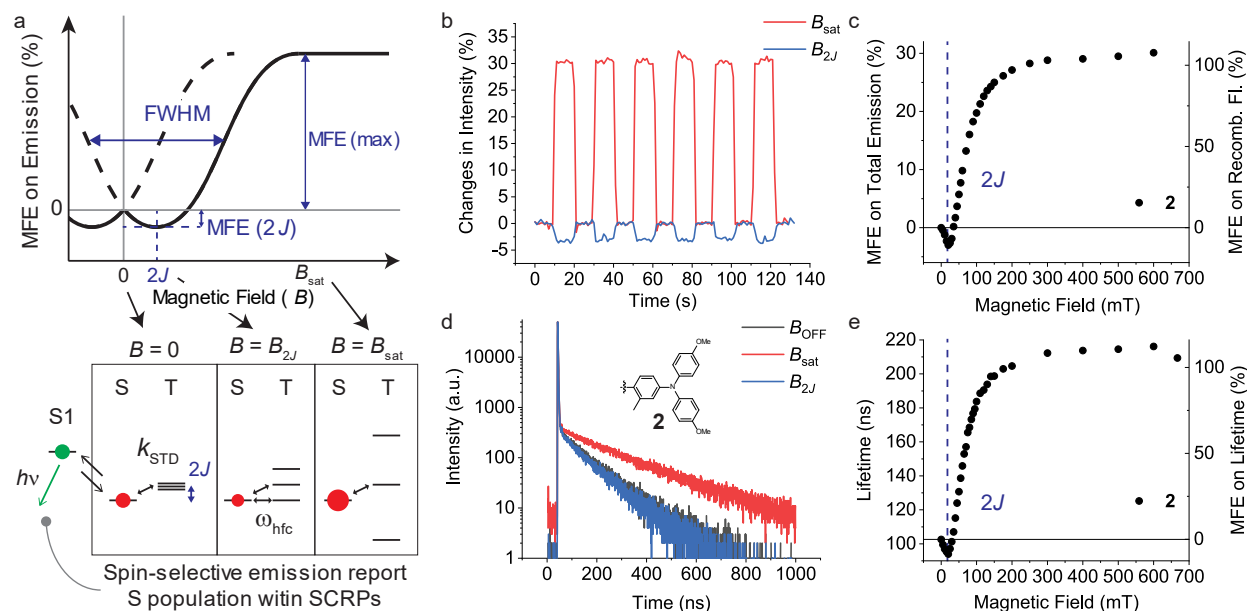
Fig. 2: Magnetic modulation of optical properties. a, General MARY curve and the key parameters for the singlet-born SCRPs system. MFEs are recorded on the emission from singlets (S1). The lower panel depicts the relative changes of the population of the singlet RPs at three different magnetic field for the case of $|2J| > B_{eff}$. **b**, Magnetic modulation of steady-state emission (total emission) at B_{2J} and B_{sat}. The emission decreases and increases at B_{2J} at B_{sat}, respectively, following the scheme in panel **a**. **c**, MFEs on total emission (left axis) and on recombination fluorescence only (right axis). $\mathrm{MFE}\,(\%) = [1 - \frac{I(B=ON)}{I(B=OFF)}] \times 100$ where I is the intensity of emission. **d**, Emission decay traces of **2** at B_{OFF}, B_{sat}, and B_{2J}. The emission contrasts increase at later times. **e**, Magnetic modulation of recombination fluorescence lifetime (left axis) and its MFEs (right axis). $\mathrm{MFE}\,(\%) = [1 - \frac{\tau(B=ON)}{\tau(B=OFF)}] \times 100$ where τ is the lifetime. All the measurements were performed in deoxygenated anisole at room temperature.

We characterized the sensitivity toward the magnetic field strengths by emission-based magnetically affected reaction yield (MARY) spectroscopy (**Fig. 2a**). A MARY curve, based on the total emission intensity and recombination fluorescence, is reported in **Fig. 2c** for molecule **2**, and the rest are reported in Supplementary Figs. 22-23: $\mathrm{MFE}\,(\%) = [1 - \frac{I(B=ON)}{I(B=OFF)}] \times 100$ where I is the emission intensity. At the saturated field (B_{sat}), the change of the total emission intensity reaches up to 30%, which far exceeds our previous molecules[10] and the modulation achieved by the NV centers without microwave excitation.[22] MFEs on recombination fluorescence become

negative at the resonance field, which reflects the exchange interaction ($2J$) or field response range of the molecular qubits.[3, 10] We did not assign a sign to $2J$ as the experiments were performed in solutions. Based on the recombination fluorescence intensity only, MFE exceeds 100 – 200 % at B_{sat} (**Fig. 2c**, and Supplementary Fig. 23). The large MFEs on recombination fluorescence intensity indicate a large change in the RPs lifetime. We recorded the MARY curves based on emission lifetimes, which are reported in **Figs. 2d-e**, Supplementary Fig. 24. Indeed, the recombination fluorescence lifetime is modulated by > 200% (e.g., **8** and **9**). We also performed the MFEs on the decays of the radicals (TAA$^{\bullet+}$) on **1** and **2**, where we could observe their dynamics clearly (Supplementary Figs. 25-26). Their MFEs correlate well with the MFEs on the emission measurements. We also determined MFEs on the formation of triplets (^{T}BD*).[23] As we demonstrated before,[10] MFEs on the production of ^{T}BD* show the opposite signs to those of MFEs based on emission, confirming the RP mechanism (**Fig. 2a**). The spectra are shown in Supplementary Fig. 27. We did not characterize MARY curves for **6**-**8** based on triplets because of little formation.

The key properties of the MARY spectra[3] are reported in **Table 2**. Magnitudes are reported at B_{sat} and B_{2J} (where observed) as MFE (max) and MFE ($2J$), respectively. We used Schulten-Wolynes (SW) theory together with Nakajima-Zwanzig spin-relaxation[24, 25, 26] to fit the MARY curves of the emission lifetimes and triplet yields when available, simultaneously. Initial parameter fitting was performed with the Fay & Manolopoulos kinetic master (KM) equations.[27] The rotational correlation times (τ_C) needed to describe spin relaxation were experimentally determined by time-resolved emission anisotropy measurements (Supplementary Note 3, Supplementary Figs. 28-29, Supplementary Table 6). Overall, we obtained better fits of the MARY curves with the SW/NZ equation, especially those with $|2J| < B_{eff}$ (the effective hyperfine coupling), and therefore used the values from the SW/NZ equation. The fits provided $|2J|$, the rate constants of singlet-triplet dephasing (STD, k_{STD}) and spin-selective charge recombination processes (k_S, and k_T). These rate constants are reported in Supplementary Table 3 and are discussed below. The fits also showed little direct production of triplets (^{S}RP → T1). The linewidth was determined by fitting the MARY spectra using two Lorentzian curves with $2J$ of opposite signs. The reported values are the FWHM of one Lorentzian (**Fig. 2a**).

To examine the effect of bridge chirality, we also synthesized the opposite chirality of **1** (**10**-(*S*)), which exhibits identical photophysical properties and MFEs. This shows the chirality of the bridge does not play a role in MFEs in solution state.

Table 2 MFEs and associated spin properties of the D-χ-A molecules.[a]

	MFE (max) (%)			MFE (2J) (%)			2J (mT)[b]	Linewidth (mT)[c]
	Total[d]	RF[e]	Life[f]	Total[d]	RF[e]	Life[f]		
1	22	35	35	-3.7	-7.4	-5	58	68
2	30	107	111	-3	-3	-8	27	44
3	9	98	90	-0.1	-3.8	-2	9.8	26
4	3.6	204	142	-0.2	0[f]	-4	0.1	27
5	27	112	117	-1.7	-10	-11	20	39
6	0.5	81	51	0[g]	0[g]	-3	0.6	38
7	2.4	170	142	0[g]	0[g]	0[g]	0.7	19
8	3.3	230	207	0[g]	0[g]	0[g]	1.2	20
9	12	136	234	-0.1	-8	-6	7.0	25

[a] Measured in deoxygenated anisole. [b] The reported values are based on the fitting to the SW equation (see **Methods**). [c] The reported values are based on the Lorentzian fitting of the MARY curves of the recombination fluorescence lifetime. [d] Total = total emission intensity. [e] RF = recombination fluorescence. [f] Life = Recombination fluorescence lifetime. [g] We did not quantify the effects, and therefore listed them as 0.

Electron transfer rates

We first discuss the rates of electron transfer reactions briefly. The efficiency of the initial charge separation depends on the donors, ranging from very low ~3% (**6**) to moderate ~70% (**1**). The charge separation, back charge recombination, and triplet recombination (k_{CS}, k_{bCR}, and k_T) generally decrease as r_{DA} increases, while k_S does not show clear distance dependency (Supplementary Fig. 30, Supplementary Note 1). We typically have $k_{CS} > k_T > k_{bCR} \sim k_S$. A faster k_T is likely facilitated by a smaller energy gap ($|\Delta G_{CRS}| \gg |\Delta G_{CRT}|$).

Molecular engineering

A molecular qubit's advantage lies in their synthetic tunability. We show how we can synthetically tune the three key parameters of magnetic sensitivity: 2J, magnitude (% MFE), and linewidth. We focused on the donor site and tested three structural modifications on the TAA core: torsional locking, distance extension, and planarization (**Fig. 1b**). Another approach is to adjust the energy

of RPs.[10] We will report this aspect on the current motif in a separate paper. We did not explicitly change the energy levels of RPs, and they differ only by 5 meV (**Table 1**). The changes in the energetics with the chemical modifications were small (Supplementary Tables 3-4). In the following, we discuss what molecular descriptors contribute to the magnetic sensitivity of molecular qubits and illustrate the ways to achieve synthetic control.

2*J*

2*J* defines the field response range. Using the Anderson's framework,[28, 29] we can express 2*J* of the current system as

$$2J = \frac{|V_{\mathrm{RP-S}}|^2}{\Delta E_{\mathrm{RP-S}}} - \frac{|V_{\mathrm{RP-T}}|^2}{\Delta E_{\mathrm{RP-T}}} \tag{1}$$

where $\Delta E_{\mathrm{RP}} = E_{\mathrm{RP}} - E_{\mathrm{n}} - \lambda_{\mathrm{T}}$. E_{RP}, E_{n}, and λ_{T} are the energies of the RP state, the surrounding local states (E_{S1} or E_{T1}), and the total reorganization energies. $V_{\mathrm{RP-S}}$ and $V_{\mathrm{RP-T}}$ are the singlet and triplet electronic couplings. We excluded the contributions from the excited states of TAA as E ($^{\mathrm{T1}}$TAA*) and E ($^{\mathrm{S1}}$TAA*) = 3.0 eV and > 4.0 eV.[30] See Supplementary Note 4 for details. Provided $\Delta E_{\mathrm{RP-S}} < 0$ and $\Delta E_{\mathrm{RP-T}} > 0$, both couplings contribute to 2*J* in the same manner; when V_{RP} increases, |2*J*| increases. Equation 1 suggests 2*J* < 0 for our molecules, but the absolute sign is not determined. Based on the McConnell model,[31, 32] we can express the coupling as

$$V_{\mathrm{RP}} = \frac{V_{\mathrm{DB}} V_{\mathrm{BA}}}{\Delta\varepsilon} \tag{2}$$

where V_{DB} and V_{BA} are the electronic couplings of donor-bridge and bridge-acceptor, and $\Delta\varepsilon$ is the tunneling energy gap. Here, we keep V_{DA} and $\Delta\varepsilon$ constant and modify V_{DB}.

Equation 1 suggests that the decrease in V_{RP}, while keeping ΔE_{RP} constant, results in a decrease in |2*J*|. Assuming the superexchange mechanism, elongation can decrease V_{RP} as $V_{\mathrm{RP}} \propto e^{-\beta r_{\mathrm{DA}}}$ where β is an exponential decay constant. We plotted the |2*J*| as a function of r_{DA} in **Fig. 3a**, where r_{DA} is computationally estimated as an electron-hole distance of the RP states (**Table 1**). Simple elongation, (Ph)$_n$ series from **1** to **3** to **6,** shows a decrease in |2*J*| with β = 0.45 Å^{-1} and confirms the earlier study by Wasielewski and co-workers (β = 0.37 Å^{-1} for their (Ph)$_n$ series).[33] Yet, as shown in **Fig. 3a**, the distance alone cannot capture the entire picture.
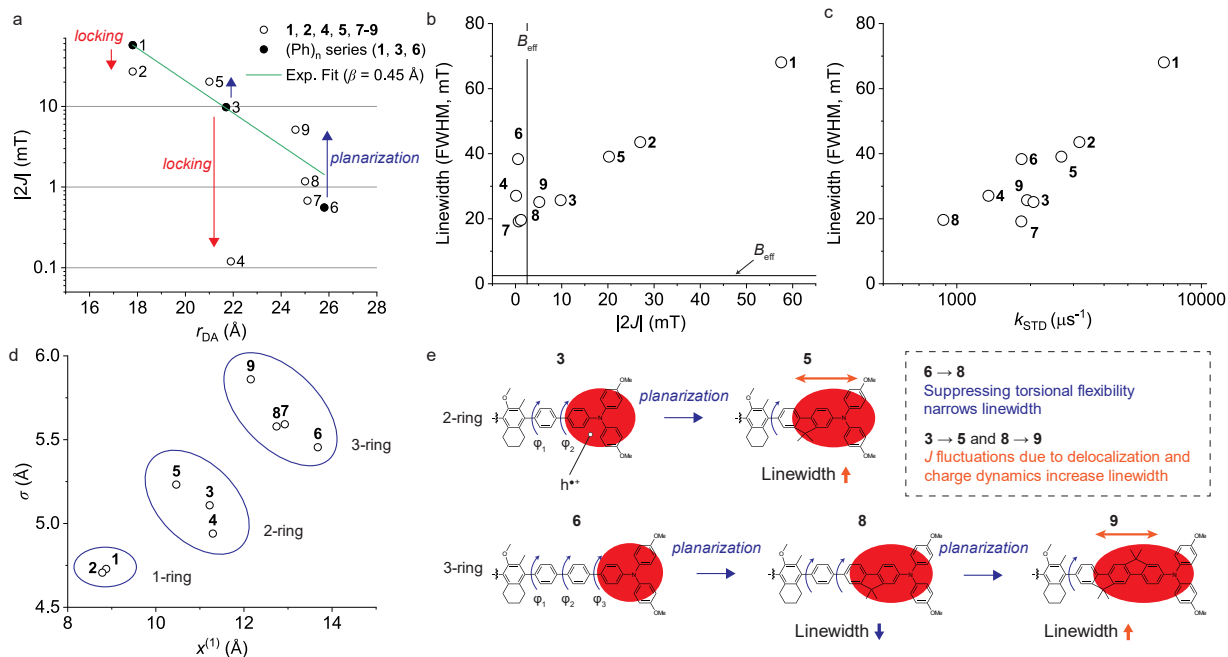
Fig. 3: Synthetic control of the key spin parameters (2*J* and linewidth). **a,** Distance dependence of |2*J*|. **b,** Relation between the linewidth and |2*J*|. The solid black lines represent the effective hyperfine coupling, B_{eff}. **c,** Relation between the linewidth and k_{STD}. **d,** The computed halfwidth (σ) and the centroid ($x^{(1)}$) of the positive charge in the D-χ-A molecules. **e,** Schematic illustration of the effects of planarization on the size of the charges and on the linewidth. The red circle indicates a hole distribution (h•+). Planarization can suppress torsional flexibility (φ_i where i = 1-3), which decreases STD (and therefore linewidth). It can also lead to the increase in 2*J* fluctuations due to delocalization and possibly charge dynamics, amplifying STD (equation 4), and therefore linewidth.

We observed the changes in |2*J*| associated with torsional locking (generally, torsion angle change),[34] which can modulate V_{RP} as $V_{RP}(\varphi)$.[35] We introduced a methyl substitution that locks the angle between BINOL and TAA to more orthogonal configurations (e.g., **1** vs **2** and **3** vs **4**). The potential energy surface calculations show the energy barrier to nonorthogonal conformations becomes steeper in **2** (Supplementary Fig. 31). This locking, highlighted yellow in **Fig. 3a**, lowers the average V_{RP}, lowering |2*J*| (e.g., 58 mT vs 27 mT for **1** vs **2**). The effect is more pronounced for the two-ring system, **3** vs **4**, possibly due to larger charge changes based on the moment's analysis (see **Methods**, **Fig. 3d**).

Planarization reduces torsional flexibility in TAAs. This acts in the opposite direction to reduction of torsional flexibility by locking with a methyl group (i.e., increase $|2J|$), as shown by blue arrows in **Fig. 3a**. The observed change is greater than the expected change from a smaller r_{DA} shift with planarization. Planarization shifts the centroid of the radical cation closer to the bridge, increasing delocalization (**Fig. 3d**). Skewness indicates charge delocalization toward the bridge (Supplementary Table 7). Thus, planarization favors conformations with a larger V_{RP}, leading to a dramatic increase of $|2J|$ in **9** vs **6**-**8**.

Linewidth

As a general trend, the linewidth (**Table 2**) becomes smaller for smaller $|2J|$ (**Fig. 3b**). The FWHM of MARY curves is expected to be B_{eff} and $\sqrt{2}B_{eff}$, for those with $|2J| < B_{eff}$ and $> B_{eff}$, respectively, when spin mixing is governed only coherently by the hyperfine interaction.[36] The calculated B_{eff} is ~2.4 mT (Supplementary Table 8). The observed linewidths are larger than these limits, indicating the contribution from S-T dephasing. Indeed, overall, the linewidth decreases with decreasing k_{STD} (linewidth ~ k_{STD}, **Fig. 3c**). Miura[36] proposed fluctuations of $|2J|$ result from torsional dynamics of bridge and associated couplings changes (non-Condon effect[37, 38, 39]). To account for these fluctuations, we can express k_{STD}, following the idea by Hore and co-workers[40]

$$k_{STD} \propto 4\langle [J(c(t)) - J_{av}]^2 \rangle \tau_c \tag{3}$$

where $J(c)$ is the conformational dependent J, where c can be a reaction coordinate (e.g., r_{DA} and torsion angle φ), τ_c is the correlation time of the $J(c)$ fluctuations, and $\langle \cdots \rangle$ indicates a time average, $J_{av} = \langle J(c(t)) \rangle$ that is $|2J_{av}| = |2J|$ experimentally determined. Here, we examined this fluctuation effect by looking at how methyl locking and planarization affect the linewidth. Methyl locking narrows the torsional distribution, especially in the one-ring system, reducing STD and linewidths (**1** to **2**). However, the effect is less clear for the two-ring system (**3** to **4**), suggesting that torsional flexibility between BINOL and the first phenyl ring (φ$_1$) dominates over the torsional restriction between two phenyls (φ$_2$) (**Fig. 3e**).

Planarization's effect on linewidth is not just linked to the number of flexible torsion angles. For the three-ring system (**6** to **7**, **8**, and **9**), linewidth decreases with planarization (**Fig. 3b**), but the most planar molecule, **9**, does not exhibit the narrowest linewidth. Similarly, contrary to our prediction, the linewidth increases for the two-ring system (**3** to **5**). This is likely because planarization significantly increases the spin-density delocalization with the TAA in these cases, as evident from the increase in $|2J|$ (for **3** to **5** and **7** to **9**). The increased delocalization also increases the typical magnitude of $J(c(t))$ fluctuations, and therefore also increases the

11

magnitude $\langle [J(c(t)) - J_{av}]^2 \rangle$ and thus k_{STD}. Spatial charge fluctuations could also contribute to the unexpected dependence of linewidth on planarization. Studies established a dynamic picture of charges associated with torsional and vibrational movements.[41, 42, 43] Planarization allows positive charge movement within the TAA moiety (i.e., fluctuations in r_{DA}), despite a rigid structure (**Fig. 3e**). This electronic heterogeneity would also contribute to a larger $\langle [J(r_{DA}(t)) - J_{av}]^2 \rangle$ term, where c(t) = r_{DA}(t), in equation 4. Thus, we observed larger k_{STD} and linewidths for molecules **5** and **9** than **4** and **8**, respectively. This is similar to line broadening seen in SCRPs in cryptochrome due to electron hopping.[44]

Magnitudes

We turn our attention to the magnitude of the MFEs on emission at B_{sat}, both steady-state and time-resolved (**Table 2**). The data shows higher signal contrasts when using emission lifetime or with time-gated counts which reduces background signals better than steady-state (**Fig. 2d**).
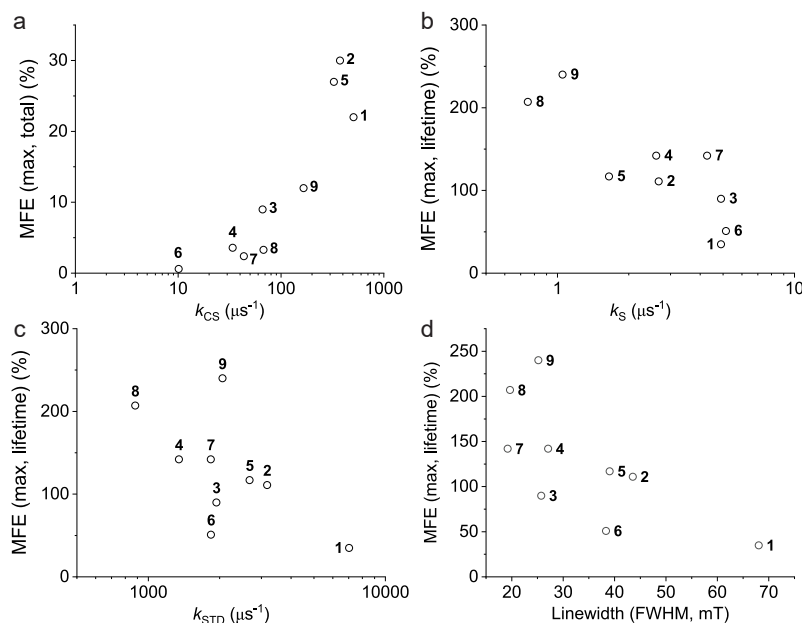

Fig. 4: Synthetic control of the key spin parameter (magnitude). **a**, Acceleration of initial charge separation (k_{CS}) increases MFE (max) on the total emission intensity. **b**, Deceleration of the singlet charge recombination (k_S) increases MFE (max) on the recombination fluorescence lifetime. **c**, Suppression of STD (k_{STD}) can increase MFE (max) on the recombination fluorescence lifetime. **d**, Relation between MFE (max) on recombination fluorescence lifetime and the linewidth. We can achieve larger MFEs while keeping linewidth small.

The steady-state MFE depends on the rate constants, with faster k_{CS} maximizing the effect (**Fig. 4a**). However, time-resolved MFEs correlate more with singlet charge recombination and STD rates than charge separation (Supplementary Fig. 32). Slowing k_S and suppressing STD increases MFEs on emission lifetime (**Fig. 4b, c**). In the current series, a planar phenyl group attached to an amine (**5**, **8**, **9**) helps delocalize charges, reducing reorganization energy,[45] pushing k_S into the Marcus inverted region to slow down k_S.[46, 47] Therefore, structural rigidification can be an effective strategy to suppress k_S and improve MFEs when such a modification could also limit charge movement. Further discussions are in Supplementary Note 4.

Synthetic control of these parameters is not mutually exclusive. Our data demonstrate we can simultaneously achieve high magnitudes (time-resolved MFEs) and lower linewidth (**Fig. 4d**). Although the current dataset is limited in size, it highlights significant opportunities for improvement. We conclude that further structural rigidification, charge delocalization, and accelerating charge separation will likely lead to higher magnitudes with lower linewidth than currently achieved.

Conclusions

In this article, we demonstrated the molecular engineering of emissive SCRPs-based molecular qubits. The molecules possess desired features, such as visible light absorption and emission, as molecular qubits for sensing and control applications. The work demonstrates the modularity in our design. The analysis, enabled by the multitudes of spectroscopic, computational, and theoretical methods, shows concrete ways for practical molecular engineering and further improvements within the current D-χ-A motif and beyond. Our findings bring photo-generated SCRPs-based molecular qubits closer to QIS applications, exploiting MFEs on emission and chemical reactivities.

Methods

1. General

All reagents and solvents were sourced from standard commercial chemical supply companies, unless noted otherwise. Silica gel (pore size 60 Å, 230–400 mesh, SiliCycle Inc.) was used in manual flash column chromatography. The ^{1}H and ^{13}C NMR spectra were recorded via a Bruker Avance III spectrometer, operating at 400 and 100 MHz, respectively, or via a Bruker Avance spectrometer, operating at 300 and 75 MHz, respectively. The ^{19}F NMR spectra were recorded via a Bruker Avance III spectrometer, operating at 376 MHz. The high resolution mass spectra were obtained via QStar Elite (AB Sciex) conducted at the Laboratory of Mass Spectrometry and Omics Analysis of the University of Connecticut Department of Chemistry. UV-vis absorption spectra were recorded by a Cary 60 Scan UV-vis spectrophotometer (Agilent). A FLS1000 photoluminescence spectrometer (Edinburgh Instruments) was used to record the steady-state and time-resolved emission. Fluorescence lifetime measurements were performed using a time-correlated single-photon counting (TCSPC) system of the FLS1000 equipped with a TCSPC/MCS/counter module (TCC2), a Hamamatsu H10720-01P, and a pulsed diode laser (EPL-510) as the excitation source that provided 506 nm excitation having a pulse duration 85 ps. Lifetime analysis with instrument response function (IRF) was performed with Fluorescence Analysis Software Technology (FAST, Edinburgh Instruments). Using the FLS1000 equipped with an integrating sphere, absolute measurements were conducted to obtain quantum yields of emission (Φ_{em}). Unless explicitly mentioned, all the photophysical characterization was conducted at room temperature (20 ^{o}C). Temperature-dependent measurements were performed with a Peltier-driven temperature-controlled cuvette holder housed in the FLS1000. Circular dichroism (CD) measurements were conducted with Applied Photophysics Pi Star-180.

2. Femtosecond Transient Absorption Spectroscopy (fs-TA)

A fs-TA system was used based on the HELIOS FIRE (Ultrafast Systems), coupled with a femtosecond laser system (Coherent). The details were reported elsewhere.[23] Datasets obtained were processed and analyzed with the software Surface Xplorer (Ultrafast Systems) via fluorescence background subtractions, applied chirp correction, time-zero adjustments, single value decomposition, global fitting, and kinetic fitting. Global fitting with sequential modeling was performed with ASUfit 3.0[48] or Ultrafast toolbox.[49] We used global fitting to analyze the data set in the spectral region from ~330 to 700 nm with a sequential, irreversible, kinetic model (A → B → C→…). The spectral profiles obtained from analysis with a sequential scheme are called

evolution-associated decay spectra (EADS).[50] While they do not necessarily result in spectra representing pure intermediate states, and rather each EADS corresponds in general to a mixture of states, it can provide a simple way of dissecting the progression of spectral changes.[51]

3. Nanosecond Transient Absorption Spectroscopy (ns-TA)

Nanosecond transient absorption (nsTA) measurements were conducted by using a system based on the LP920 (Edinburgh Instruments) coupled with a tunable nanosecond laser system (Opolette UX10230U, Opotek), Xe Model 920 450 W xenon arc lamp as the probe lamp, and a monochromator, with a P928 photomultiplier detector (Hamamatsu) for decay measurements and iCCD camera (Andor Technology) for spectral measurements, respectively. The energy of the pump beam was adjusted to ~1-2 mJ, depending on the samples, throughout the measurements. The samples were deoxygenated by bubbling the solutions with nitrogen for at least 15 minutes prior to taking measurements. A quartz cuvette with a path length of 1.0 cm was used for the measurements. Quantum yields of triplet excited states were measured using a relative actinometry method compared with the formation of triplet excited states of diiodo BODIPY in toluene (Φ_T = 0.88).[52, 53] Datasets were analyzed using OriginPro 2017 (OriginLab Corporation).

4. Electrochemistry

Cyclic voltammetry measurements were conducted on all molecules based on a 600E Electrochemical Analyzer/Workstation (CH Instruments). This system was equipped with a standard three-electrode cell comprised of a pseudo-Ag reference electrode, a Pt wire counter electrode, and a 3 mm glassy carbon-disk working electrode in an acetonitrile (MeCN) solution of 0.1 M tetrabutylammonium hexafluorophosphate ($TBA^+PF_6^-$). Datasets were processed and analyzed with the software CHI600e (CH Instruments). Measured potentials are referenced vs. $Fc^{+/0}$; ferrocene was introduced before measurements were conducted. Spectroelectrochemical measurements were performed with a honeycomb spectroelectrochemical cell (PINE research) coupled to the 600E Electrochemical Analyzer/Workstation. Samples were prepared in MeCN with 0.1 M $TBA^+PF_6^-$.

5. Computations

Computations for energetics and moments analysis were carried out with *Gaussian16*.[54] The geometries were optimized with B3LYP[55, 56] functional in density functional theory (DFT) calculations. B3LYP correctly predicts the energy order of singlets, RPs, and triplets in these systems although we did not perform exhaustive search for optimal functionals. All calculations

on cation radicals were spin-unrestricted. The 6-31+G(d) basis set was used for the geometry optimization and TDDFT single-point energy calculations. Hexyl chains of molecule **9** were replaced by methyl groups. The conductor-like polarizable continuum model (CPCM)[57, 58] (anisole) was used as implemented in *Gaussian*.

Computations for spin properties on BD and TAAs were carried out with Orca 5.03.[59, 60] The geometries were optimized at the level of ωB97X-D3[61, 62, 63]/def2-SVP with CPCM (chloroform) as implemented in Orca. Hyperfine tensors and *g*-tensors were obtained from single point calculations at the level of ωB97X-D3/EPR-III with CPCM (chloroform) where spin-orbit couplings are treated with Z_{eff} model. The effective hyperfine couplings, B_{eff}, were calculated by $B_{eff} = \sqrt{B_{BD^{\bullet-}}^2 + B_{TAA^{\bullet+}}^2}$ where $B_{BD^{\bullet-}}$ and $B_{TAA^{\bullet+}}$ are the hyperfine coupling s of BD$^{\bullet-}$ and TAA$^{\bullet+}$, respectively.

Moment's analysis was performed on the radical cations of D-χ-A molecules, assuming the radical cations alone behave in a similar manner to those in the RPs. The full procedures were described earlier.[64, 65] Briefly, the atomic charges were derived from a least-squares fit to the electrostatic potential calculated with the "Charges from electrostatic potentials using a Grid" (CHelpG) scheme[66] as implemented in *Gaussian16*. The centroid ($x^{(1)}$), half-width (σ), and skewness (γ) of the excess electrons based on the differences of electrostatic potential (ESP) charge distributions (the long axis of the molecule, and in the axis of electron transfer reactions) between the radical cations and neutrals were determined. We determined these parameters for a given cation radical, based on the change in charge density ($\Delta\rho$) when the cation radical is formed from the neutral species, taking account of the corresponding modest change in equilibrium coordinates. This approach is based on the idea that the width (2σ) can be described as suitable second moments of the state charge densities, as discussed by Newton et al.[67] All the reported centroids are referenced to the center of mass of compound **1**.

6. MARY Measurements and Fittings

Fluorescence-based MARY spectroscopy setup consists of an electromagnet (3470, GMW Associates) and the FLS1000 spectrometer (Edinburgh). Excitation and emission lights were guided to and from the electromagnet using a fiber launcher. The electromagnet has axial holes in each pole (8 mm) and was equipped with a power supply (BOP50-8ML) and cooled using a recirculating chiller (Isotemp II, Fisher Scientific). The magnetic field was calibrated by a gaussmeter (Model 475 DSP, Lakeshore). For steady-state measurements, the fields were

usually altered between 0 ('off') and the target field B ('on') every 10 seconds, controlled by an in-house software. The MFEs were calculated as the average of at least five on/off measurements. The 'on' and 'off' intensities were automatically selected based on when the magnet was activated or deactivated, with the timing accurately identified by the in-house software according to the measurement conditions. MFE on recombination fluorescence was determined using the fraction of recombination fluorescence based on the relative contribution of the emission lifetimes at each field. For emission lifetime measurements, the measurements were alternatively performed at 0 and the target field B. In both steady-state and time-resolved measurements, the emission was collected at a 90° angle relative to the excitation light, rejecting excess stray lights. Steady-state and time-resolved emission measurements were performed with λ_{ex} = 480 nm (provided by a Xe lamp) and 506 nm (provided by a diode laser), respectively. TA-based MARY spectroscopy setup consists of the same electromagnet and the LP920. The detail of the setup is described above. The kinetic measurements at select wavelengths were performed alternatively at 0 and the target field B.

The magnetic field effects on fluorescence lifetime and triplet yield were simulated using the Schulten-Wolynes/Nakajima-Zwanzig (SW/NZ) method from Ref. [24]. The Haberkorn radical pair master equation was solved replacing the quantum spin operators of hyperfine coupled nuclear spins with semi-classical vectors, and spin relaxation due to diffusive rotational modulation of hyperfine, dipolar and g-tensors was accounted for using the Nakajima-Zwanzig approach. Singlet-triplet dephasing was accounted with a Lindblad type dephasing operator with phenomenological rate k_{STD}. This approach accounts accurately for spin-relaxation and hyperfine effects across a wide parameter regime.[68] Hyperfine tensor and g-tensors needed in the method were calculated as given above. Relaxation was treated with a prolate top model using the experimental τ_c to describe rotation perpendicular to the symmetry axis, and a correlation time of 150 ps was used for diffusion about the symmetry axis, roughly corresponding to the correlation time for free BD. A four-parameter fit was performed for each molecular to both radical pair lifetime and the relative triplet yield (where available), with the singlet and triplet recombination rates (k_S and k_T), the J coupling and singlet-triplet dephasing rate (k_{STD}) treated as fitting parameters. An initial global parameter search was performed using the less accurate but more computationally efficient kinetic master equation (KME) method from Ref. [27], the result of which was used to fit the MFE data using the SW/NZ method. The fits are shown in Supplementary Figs. 33-34.

Data availability

All relevant data are available within the paper and its Supplementary Information files.

References

1. Wasielewski MR, Forbes MDE, Frank NL, Kowalski K, Scholes GD, Yuen-Zhou J*, et al.* Exploiting chemistry and molecular systems for quantum information science. *Nat Rev Chem* 2020, **4**(9)**:** 490-504.

2. Harvey SM, Wasielewski MR. Photogenerated Spin-Correlated Radical Pairs: From Photosynthetic Energy Transduction to Quantum Information Science. *J Am Chem Soc* 2021, **143**(38)**:** 15508-15529.

3. Mani T. Molecular qubits based on photogenerated spin-correlated radical pairs for quantum sensing. *Chem Phys Rev* 2022, **3**(2)**:** 021301.

4. Nelson JN, Zhang J, Zhou J, Rugg BK, Krzyaniak MD, Wasielewski MR. CNOT gate operation on a photogenerated molecular electron spin-qubit pair. *J Chem Phys* 2020, **152**(1)**:** 014503.

5. Schirhagl R, Chang K, Loretz M, Degen CL. Nitrogen-Vacancy Centers in Diamond: Nanoscale Sensors for Physics and Biology. *Annu Rev Phys Chem* 2014, **65**(1)**:** 83-105.

6. Bayliss SL, Laorenza DW, Mintun PJ, Kovos BD, Freedman DE, Awschalom DD. Optically addressable molecular spins for quantum information processing. *Science* 2020, **370**(6522)**:** 1309-1312.

7. Fataftah MS, Bayliss SL, Laorenza DW, Wang X, Phelan BT, Wilson CB*, et al.* Trigonal Bipyramidal V3+ Complex as an Optically Addressable Molecular Qubit Candidate. *J Am Chem Soc* 2020, **142**(48)**:** 20400-20408.

8. Yu C-J, Krzyaniak MD, Fataftah MS, Wasielewski MR, Freedman DE. A concentrated array of copper porphyrin candidate qubits. *Chem Sci* 2019, **10**(6)**:** 1702-1708.

9.   Graham MJ, Zadrozny JM, Fataftah MS, Freedman DE. Forging Solid-State Qubit Design Principles in a Molecular Furnace. *Chem Mater* 2017, **29**(5)**:** 1885-1897.

10.   Buck JT, Mani T. Magnetic Control of Recombination Fluorescence and Tunability by Modulation of Radical Pair Energies in Rigid Donor–Bridge–Acceptor Systems. *J Am Chem Soc* 2020, **142**(49)**:** 20691-20700.

11.   Steiner UE, Ulrich T. Magnetic-Field Effects in Chemical-Kinetics and Related Phenomena. *Chem Rev* 1989, **89**(1)**:** 51-147.

12.   Cao H, Fujiwara Y, Haino T, Fukazawa Y, Tung C-H, Tanimoto Y. Magnetic Field Effects on Intramolecular Exciplex Fluorescence of Chain-Linked Phenanthrene and N,N-Dimethylaniline: Influence of Chain Length, Solvent, and Temperature. *Bull Chem Soc Jpn* 1996, **69**(10)**:** 2801-2813.

13.   Cao H, Miyata K, Tamura T, Fujiwara Y, Tanimoto Y, Okazaki M*, et al.* Effect of a high magnetic field on the decay rate of chain-linked intramolecular exciplex fluorescence. *Chem Phys Lett* 1995, **246:** 171.

14.   Lee H, Yang N, Cohen AE. Mapping Nanomagnetic Fields Using a Radical Pair Reaction. *Nano Lett* 2011, **11**(12)**:** 5367-5372.

15.   Yang N, Cohen AE. Optical imaging through scattering media via magnetically modulated fluorescence. *Opt Express* 2010, **18**(25)**:** 25461-25467.

16.   Eckvahl HJ, Copley G, Young RM, Krzyaniak MD, Wasielewski MR. Detecting Chirality-Induced Spin Selectivity in Randomly Oriented Radical Pairs Photogenerated by Hole Transfer. *J Am Chem Soc* 2024, **146**(34)**:** 24125-24132.

17.   Eckvahl HJ, Tcyrulnikov NA, Chiesa A, Bradley JM, Young RM, Carretta S*, et al.* Direct observation of chirality-induced spin selectivity in electron donor–acceptor molecules. *Science* 2023, **382**(6667)**:** 197-201.

18.   Naaman R, Waldeck DH. Spintronics and Chirality: Spin Selectivity in Electron Transport Through Chiral Molecules. *Annu Rev Phys Chem* 2015, **66**(1)**:** 263-281.

19.   Tsuji M, Abuhadba S, Chen A, Ito M, Makhijani A, Kuwahara Y*, et al.* Red-Colored Circularly Polarized Luminescence from a Benzo-Fused BODIPY-BINOL Complex. *J Phys Chem B* 2023, **127**(45)**:** 9781-9787.

20.   Lin N, Mani T. Anti-Arrhenius behavior of electron transfer reactions in molecular dimers. *Chem Sci* 2023, **14**(45)**:** 13095-13107.

21.   Johnson S, Makhijani A, Tsuji M, Mani T. Acceleration of Nonradiative Charge Recombination Reactions at Larger Distances in Kinked Donor–Bridge–Acceptor Molecules. *J Phys Chem B* 2022, **126**(43)**:** 8851-8863.

22.   Le Sage D, Arai K, Glenn DR, DeVience SJ, Pham LM, Rahn-Lee L*, et al.* Optical magnetic imaging of living cells. *Nature* 2013, **496**(7446)**:** 486-489.

23.   Buck JT, Boudreau AM, DeCarmine A, Wilson RW, Hampsey J, Mani T. Spin-Allowed Transitions Control the Formation of Triplet Excited States in Orthogonal Donor-Acceptor Dyads. *Chem* 2019, **5**(1)**:** 138-155.

24.   Fay TP, Lindoy LP, Manolopoulos DE. Electron spin relaxation in radical pairs: Beyond the Redfield approximation. *J Chem Phys* 2019, **151**(15).

25.   Fay TP, Lindoy LP, Manolopoulos DE. Spin-selective electron transfer reactions of radical pairs: Beyond the Haberkorn master equation. *J Chem Phys* 2018, **149**(6).

26.   Schulten K, Wolynes PG. Semiclassical description of electron spin motion in radicals including the effect of electron hopping. *J Chem Phys* 1978, **68**(7)**:** 3292-3297.

27.   Fay TP, Manolopoulos DE. Radical pair intersystem crossing: Quantum dynamics or incoherent kinetics? *J Chem Phys* 2019, **150**(15)**:** 151102.

28.   Anderson PW. New Approach to the Theory of Superexchange Interactions. *Phys Rev* 1959, **115**(1)**:** 2-13.

29.   Verhoeven JW. On the role of spin correlation in the formation, decay, and detection of long-lived, intramolecular charge-transfer states. *J Photochem Photobiol C* 2006, **7**(1)**:** 40-60.

30.   Bagnich SA, Athanasopoulos S, Rudnick A, Schroegel P, Bauer I, Greenham NC*, et al.* Excimer Formation by Steric Twisting in Carbazole and Triphenylamine-Based Host Materials. *J Phys Chem C* 2015, **119**(5)**:** 2380-2387.

31.   McConnell HM. Intramolecular Charge Transfer in Aromatic Free Radicals. *J Chem Phys* 1961, **35**(2)**:** 508-515.

32.   Newton MD. Quantum Chemical Probes of Electron-Transfer Kinetics - the Nature of Donor-Acceptor Interactions. *Chem Rev* 1991, **91**(5)**:** 767-792.

33. Weiss EA, Ahrens MJ, Sinks LE, Gusev AV, Ratner MA, Wasielewski MR. Making a molecular wire: Charge and spin transport through para-phenylene oligomers. *J Am Chem Soc* 2004, **126**(17): 5577-5584.

34. Roger C, Schmiedel A, Holzapfel M, Lukzen NN, Steiner UE, Lambert C. The influence of hindered rotation on electron transfer and exchange interaction in triarylamine-triptycene-perylene diimide triads. *Phys Chem Chem Phys* 2024, **26**(6): 4954-4967.

35. Newton MD. Modeling donor/acceptor interactions: Combined roles of theory and computation. *Int J Quantum Chem* 2000, **77**(1): 255-263.

36. Miura T, Scott AM, Wasielewski MR. Electron Spin Dynamics as a Controlling Factor for Spin-Selective Charge Recombination in Donor−Bridge−Acceptor Molecules. *J Phys Chem C* 2010, **114**(48): 20370-20379.

37. Rosokha SV, Newton MD, Head-Gordon M, Kochi JK. Mulliken–Hush elucidation of the encounter (precursor) complex in intermolecular electron transfer via self-exchange of tetracyanoethylene anion-radical. *Chem Phys* 2006, **324**(1): 117-128.

38. Jang S, Newton MD. Theory of torsional non-Condon electron transfer: A generalized spin-boson Hamiltonian and its nonadiabatic limit solution. *J Chem Phys* 2005, **122**(2): 024501.

39. Berlin YA, Grozema FC, Siebbeles LDA, Ratner MA. Charge Transfer in Donor-Bridge-Acceptor Systems: Static Disorder, Dynamic Fluctuations, and Complex Kinetics. *J Phys Chem C* 2008, **112**(29): 10988-11000.

40. Kattnig DR, Sowa JK, Solov'yov IA, Hore PJ. Electron spin relaxation can enhance the performance of a cryptochrome-based magnetic compass sensor. *New J Phys* 2016, **18**(6): 063007.

41. Zamadar M, Asaoka S, Grills DC, Miller JR. Giant infrared absorption bands of electrons and holes in conjugated molecules. *Nat Commun* 2013, **4**: 2818 2811-2817.

42. Kendrick WJ, Jirásek M, Peeks MD, Greetham GM, Sazanovich IV, Donaldson PM, *et al.* Mechanisms of IR amplification in radical cation polarons. *Chem Sci* 2020, **11**(8): 2112-2120.

43. Yan J, Wilson RW, Buck JT, Grills DC, Reinheimer EW, Mani T. IR linewidth and intensity amplifications of nitrile vibrations report nuclear-electronic couplings and associated structural heterogeneity in radical anions. *Chem Sci* 2021, **12**(36): 12107-12117.

44. Golesworthy MJ, Zollitsch T, Luo J, Selby D, Jarocha LE, Henbest KB*, et al.* Singlet–triplet dephasing in radical pairs in avian cryptochromes leads to time-dependent magnetic field effects. *J Chem Phys* 2023, **159**(10).

45. Bredas JL, Beljonne D, Coropceanu V, Cornil J. Charge-transfer and energy-transfer processes in pi-conjugated oligomers and polymers: A molecular picture. *Chem Rev* 2004, **104**(11)**:** 4971-5003.

46. Marcus RA. On the Theory of Oxidation-Reduction Reactions Involving Electron Transfer .1. *J Chem Phys* 1956, **24**(5)**:** 966-978.

47. Jortner J. Temperature dependent activation energy for electron transfer between biological molecules. *J Chem Phys* 1976, **64**(12)**:** 4860-4867.

48. Schulte T, Niedzwiedzki DM, Birge RR, Hiller RG, Polívka T, Hofmann E*, et al.* Identification of a single peridinin sensing Chl-*a* excitation in reconstituted PCP by crystallography and spectroscopy. *Proc Natl Acad Sci USA* 2009, **106**(49)**:** 20764-20769.

49. van Wilderen LJGW, Lincoln CN, van Thor JJ. Modelling Multi-Pulse Population Dynamics from Ultrafast Spectroscopy. *Plos One* 2011, **6**(3)**:** e17373.

50. van Stokkum IHM, Larsen DS, van Grondelle R. Global and target analysis of time-resolved spectra. *Biochim Biophys Acta Bioenerg* 2004, **1657**(2)**:** 82-104.

51. Pan J, Lin S, Allen JP, Williams JC, Frank HA, Woodbury NW. Carotenoid Excited-State Properties in Photosynthetic Purple Bacterial Reaction Centers: Effects of the Protein Environment. *J Phys Chem B* 2011, **115**(21)**:** 7058-7068.

52. Wang Z, Zhao J. Bodipy–Anthracene Dyads as Triplet Photosensitizers: Effect of Chromophore Orientation on Triplet-State Formation Efficiency and Application in Triplet–Triplet Annihilation Upconversion. *Org Lett* 2017, **19**(17)**:** 4492-4495.

53. Ly JT, Presley KF, Cooper TM, Baldwin LA, Dalton MJ, Grusenmeyer TA. Impact of iodine loading and substitution position on intersystem crossing efficiency in a series of ten methylated-meso-phenyl-BODIPY dyes. *Phys Chem Chem Phys* 2021, **23**(21)**:** 12033-12044.

54. Frisch MJ, Trucks GW, Schlegel HB, Scuseria GE, Robb MA, Cheeseman JR*, et al.* Gaussian 16 Rev. B.01. Wallingford, CT; 2016.

55. Becke AD. Density-Functional Thermochemistry. III. The Role of Exact Exchange. *J Chem Phys* 1993, **98**(7)**:** 5648-5652.

56.   Stephens PJ, Devlin FJ, Chabalowski CF, Frisch MJ. Ab-Initio Calculation of Vibrational Absorption and Circular-Dichroism Spectra Using Density-Functional Force-Fields. *J Phys Chem* 1994, **98**(45)**:** 11623-11627.

57.   Barone V, Cossi M. Quantum Calculation of Molecular Energies and Energy Gradients in Solution by a Conductor Solvent Model. *J Phys Chem A* 1998, **102**(11)**:** 1995-2001.

58.   Cossi M, Rega N, Scalmani G, Barone V. Energies, structures, and electronic properties of molecules in solution with the C-PCM solvation model. *J Comput Chem* 2003, **24**(6)**:** 669-681.

59.   Neese F. Software update: The ORCA program system—Version 5.0. *Wiley Interdiscip Rev Comput Mol Sci* 2022, **12**(5)**:** e1606.

60.   Neese F. The ORCA program system. *Wiley Interdiscip Rev Comput Mol Sci* 2012, **2**(1)**:** 73-78.

61.   Chai J-D, Head-Gordon M. Long-range corrected hybrid density functionals with damped atom-atom dispersion corrections. *Phys Chem Chem Phys* 2008, **10**(44)**:** 6615-6620.

62.   Lin Y-S, Li G-D, Mao S-P, Chai J-D. Long-Range Corrected Hybrid Density Functionals with Improved Dispersion Corrections. *J Chem Theory Comput* 2013, **9**(1)**:** 263-272.

63.   Grimme S, Antony J, Ehrlich S, Krieg H. A consistent and accurate ab initio parametrization of density functional dispersion correction (DFT-D) for the 94 elements H-Pu. *J Chem Phys* 2010, **132**(15).

64.   Mani T, Grills DC, Newton MD, Miller JR. Electron Localization of Anions Probed by Nitrile Vibrations. *J Am Chem Soc* 2015, **137**(34)**:** 10979-10991.

65.   Boudreau AM, Wilson RW, Yang M, Grills DC, Mani T. Vibrational Spectroscopy Reveals Effects of Electron Push–Pull and Solvent Polarity on Electron Delocalization in Radical Anions of Donor–Acceptor Compounds. *J Phys Chem B* 2020, **124**(8)**:** 1543-1549.

66.   Breneman CM, Wiberg KB. Determining Atom-Centered Monopoles from Molecular Electrostatic Potentials - the Need for High Sampling Density in Formamide Conformational-Analysis. *J Comput Chem* 1990, **11**(3)**:** 361-373.

67.   Cave RJ, Edwards ST, Kouzelos JA, Newton MD. Reduced Electronic Spaces for Modeling Donor/Acceptor Interactions. *J Phys Chem B* 2010, **114**(45)**:** 14631-14641.

68.   Fay TP, Lindoy LP, Manolopoulos DE. Spin relaxation in radical pairs from the stochastic Schrödinger equation. *J Chem Phys* 2021, **154**(8).